NASA CONTRACTOR REPORT

NASA CR-929

DEPLOYMENT MECHANICS FOR AN INFLATABLE TENSION-CONE DECELERATOR

by Albert C. Kyser

Prepared by
ASTRO RESEARCH CORPORATION
Santa Barbara, Calif.
for Langley Research Center

NATIONAL AERONAUTICS AND SPACE ADMINISTRATION • WASHINGTON, D. C. • NOVEMBER 1967

NASA CR-929

DEPLOYMENT MECHANICS FOR AN INFLATABLE

TENSION-CONE DECELERATOR

By Albert C. Kyser

NATIONAL AERONAUTICS AND SPACE ADMINISTRATION

ABSTRACT

The results of an experimental development of a deployable
tension-cone decelerator are presented. The design makes use
of an inflatable toroid for the compression-resistant structure
in the base of the cone. Toroids of two different slenderness
ratios were subjected to radial compressive loads to determine
the resistance to buckling and the post-buckling behavior under
static loads. Measurements were made of the large deformation
bending moment developed by the folding hinge of an inflatable
tube. The results of these tests were incorporated in an anal-
ysis of the loads on the folded aft ring of a tension-cone de-
celerator. Finally, deployment tests were made by towing the
decelerator underwater and the results were found to correlate
reasonably well with the elementary theory.

TABLE OF CONTENTS

DEPLOYMENT MECHANICS FOR AN INFLATABLE TENSION-CONE DECELERATOR

By Albert C. Kyser

Astro Research Corporation

SUMMARY

This report describes some of the results of an experimental development of a deployable tension-cone decelerator. The design which is considered here makes use of an inflatable toroid for the compression-resistant structure in the base of the cone. Toroids of two different slenderness ratios were subjected to radial compressive loads to determine the resistance to buckling and the post-buckling behavior under static loads. Measurements were also made of the large-deformation bending moment developed by the folding "hinge" of an inflatable tube. The results of the static tests were incorporated into an elementary analysis of the loads on the folded aft ring of a tension cone decelerator during deployment. Finally, a series of deployment tests were made by towing a decelerator model underwater. The results of the deployment tests were found to correlate reasonably well with the elementary theory.

INTRODUCTION

The tension-cone decelerator concept as described in references 1 and 2 has been proposed as a solution to the problem of entry deceleration in planetary atmospheres. The concept was developed as the result of an effort to improve the weight-to-drag ratio for lightly-loaded hypersonic decelerators by improving the structural loading conditions in the decelerator cone. Thus, the large aerodynamic surface is designed in such a way that the structural loads are carried in tension to a concentrated compression-resistant structure at the base. The resulting structural configuration is capable of operating at relatively high stress, thereby permitting a reduction of structural material.

The decelerator geometry which has resulted is particularly well suited for use as a deployable hypersonic decelerator. The decelerator surface, because it is a tension element, can be foldable. Furthermore, the design of the compression-resistant structure at the base of the flexible cone is not complicated by the requirements of the aerodynamic surface. Since the aerodynamic shape is basically an apex-forward cone, the problems of opening

shock in a high "q" environment are greatly reduced and, with proper design, deployment should be possible over a wide range of conditions. These considerations suggest that effort should be expended to develop a deployable decelerator with the basic tension-cone geometry.

The aeroelastic characteristics of towed tension-cone decelerators have been examined in references 3 and 4. The present report describes some results pertinent to the development of a deployable tension-cone decelerator. Emphasis is placed on the design of the compression-resistant structure which supports the base of the cone, for which purpose an inflatable filament-wound toroidal ring has been chosen. The study attempts to answer some of the basic questions concerning the use of inflated toroids for this purpose, by examining the load-carrying ability and failure modes of such a toroid during and after deployment, and by examining the manner in which these properties affect the design of a deployable tension-cone decelerator.

SYMBOLS

A	cross sectional area of fiber, $in.^2$
C_D	drag coefficient of decelerator, referred to area of base.
C_D^*	drag coefficient of folded decelerator, referred to frontal area of folded configuration.
c	toroid slenderness parameter $r/\bar{R}$.
D	drag force, lb.
E	modulus of elasticity, lb/in^2.
$(EA)_H$	stiffness of helical fiber, lb.
$(EA)_M$	combined stiffness of meridional fibers associated with one triangular unit cell defined by the helical winding, lb.
F	resultant force, lb.
G	shear modulus, lb/in^2.
h	moment arm, in.
I	area moment of inertia of cross section, in^4

J	polar moment of inertia of cross section, in^4.
k	hoop-force-carrying capability of toroid at the final stage of deployment, as a fraction of $p\pi r^2$.
M	bending moment, lb-in.
n	number of fibers.
P	hoop force in ring.
P*	pressure stiffness parameter, $p\pi r^2 \bar{R}^2/EI$.
p	internal pressure in toroid, lb/in^2.
q	dynamic pressure, lb/in^2.
R	radius coordinate, in.
$\bar{R}$	mean radius of toroid cross-section, in.
r	mean radius of curvature of toroid meridian, in.
S	shear stiffness parameter, $\pi r \bar{R}^2 \cdot Gt/EI$
T	tension force in structural fiber, lb.
T'	tension force per unit length in the filamentary surface, lb/in.
t	effective thickness of toroid shell, in.
α	angle between tangent to meridian and axis of revolution.
β	angle in deployment-moment derivation (Figure 18).
Γ	buckling load parameter, GJ/EI.
ε	angle in deployment moment derivation (Figure 18).
η	nondimensional moment arm of resultant force on bent toroid (Figure 18).
μ	factor to account for effect of compliance of meridional fibers on bending stiffness of toroid.

θ	half-angle of bend.
θ_H	angle between helical fiber and equatorial direction.
ϕ	central angle.
Ψ	angle in deployment moment derivation (Figure 18).

Subscripts:

b	base of decelerator.
cr	critical condition for buckling
h	hub.
H	helical fibers.
M	meridional fibers.
t	tangent point between tension cone and toroid.
z	axial-direction component.

BASIC CONFIGURATION OF THE DEPLOYABLE DECELERATOR

The decelerator configuration considered here is shown in Figure 1. The aerodynamic surface is a flared conical skirt which is attached at its apex to a hub and supported radially at its base by a compression-resistant ring. The primary structural loads in the cone are carried by an array of meridional fibers which are bonded to the fabric which forms the aerodynamic surface. It is assumed that the meridional shape allows the surface to carry the aerodynamic load with zero stress in the circumferential direction. The particular shape of the curve used here is identified by the notation of reference 5 as having a shape parameter $A^2 = 1.4$. The ring at the base is a pressure-stabilized, filament-wound toroid.

The structural loads carried by the cone and the toroid are as shown in Figure 2. The aerodynamic drag force D is equilibrated at the hub by the tension in the n meridional fibers. Neglecting inertia forces of the decelerator itself, the equilibrium at the hub is seen to be

$$D = qC_D \pi R_b^2 = nT \cos\alpha_h \tag{1}$$

The hoop force in the ring depends on the manner in which the cone structure is attached. For the configuration shown in Figure 2, the hoop force P is

$$P = \frac{nT(1 + \sin\alpha_t)}{2\pi} \cong \frac{nT}{\pi} \tag{2}$$

This expression neglects the radial component of the aerodynamic load acting on the toroid surface. Assuming that the geometry is essentially as shown in Figure 2, this radial contribution from aerodynamic forces will not be important.

The hoop force P can be expressed in terms of the drag quantities by substituting for nT from equation (1).

$$P = \frac{qC_D R_b^2}{\cos\alpha_h} \tag{3}$$

For the decelerator configuration shown in Figures 1 and 2, the structural fibers of the cone extend around the toroid and are secured with a small ring on the back side. Since the toroid must provide radial support for both the back-side fibers and the meridional fibers on the cone, the radial loading on the toroid is twice that which would be required to support the meridional fibers alone (assuming that the fibers are free to slide on the toroid surface). In the interest of providing justification for this design approach, two alternate methods for terminating the meridional fibers will be considered briefly. These schemes are sketched in Figure 3.

In the configuration shown in Figure 3a, the back-side fibers are eliminated by bonding the meridional fibers to the toroid. The

resultant hoop force carried by the toroid is therefore half of that given by equation (2). The asymmetrical loading condition, however, introduces a bending stress in the toroid (as shown, for example, in reference 6). It can be shown that the stress distribution across the toroid cross section in this case is the same as that for a cylinder loaded by an eccentric, axial compressive load applied along an element of the cylinder, for which case the maximum bending stress is twice the average compressive stress due to the axial load. The maximum (combined) compressive stress in the section is therefore three times that which would result from a symmetrical load of the same size; it is one-and-a-half times as great as the stress which would be produced by balancing the eccentric load by a second load applied at the opposite edge of the cross section. Thus, the structural configuration of Figure 3a produces a maximum compressive stress in the ring which is fifty percent greater than that which occurs in the configuration of Figure 2, with the back-side fibers.

A second scheme to reduce the compressive load carried by the toroid is shown in Figure 3b. Here the cone structure is carried around the toroid and tied into itself in such a way that the back-side fibers assist in supporting the drag load. The hoop force is reduced and the toroid load is symmetrical. The difficulty with this scheme is that the back-side fibers tend to distort the aerodynamic surface by pulling the toroid forward, and increasing the curvature of the front-side fibers that support the aerodynamic surface. It has been assumed that this type of distortion is undesirable.

BUCKLING OF INFLATED TOROIDS UNDER RADIAL COMPRESSIVE LOADS

In the design of a deployable tension-cone decelerator, the most critical problems are those associated with the inflated compression-resistant toroidal ring. The ring must be designed to deploy under load and to carry the compression load without buckling. It must also be light-weight, foldable, and resistant to damage from repeated folding and deployment. In order to gain experience with this type of structure, several toroids were made and tested, and comparisons were made between the observed load-carrying ability and theoretical predictions based on isotropic shell theory. In the sections which follow, the buckling-load calculation is outlined and static-load tests are described for sample toroids loaded in radial compression.

Buckling Relations

There are at least three different possible modes of failure for a flexible, pressure-stabilized toroid loaded in the manner of the aft ring of a tension-cone decelerator. Two of these failure modes result from general instabilities corresponding to the buckling modes of slender compressively loaded rings: an in-plane buckling mode, in which the ring deforms by bending into an ellipse, and an out-of-plane buckling mode, in which the ring deforms by both

bending and twisting. The third failure mode corresponds to the local crippling of a thin-walled tube and occurs after the compressive hoop force in the ring exceeds the pressure-induced equatorial tension force.

Relations for the critical ring-buckling loads for slender, thin walled, pressurized toroidal shells subjected to a uniform radial compressive loading are given in reference 7 as follows: For in-plane buckling the hoop force P_{cr} is

$$P_{cr} = \frac{4.5EI}{\bar{R}^2} \left[1 + \frac{3}{2} c + \frac{4 + 4.5c}{S + P^*} \right]^{-1} \qquad (4)$$

For out-of-plane buckling,

$$P_{cr} = \frac{EI}{\bar{R}^2} \left[12 + \frac{1.5\Gamma}{S + P^*} \right] \left[4 + 5c + \frac{1}{\Gamma}(1 + 6.67c) \right.$$

$$\left. + \frac{1}{S + P^*}(12.375 + 13.875c) + \frac{\Gamma}{S + P^*}(0.5 + 0.833c) \right]^{-1} \qquad (5)$$

Here $\bar{R}$ = mean radius of cross section = $R_b - r$

$$c \quad = \quad r/\bar{R}$$

$$S \quad = \quad \pi r \bar{R}^2 Gt/EI$$

$$P^* \quad = \quad p \pi r^2 \bar{R}^2/EI$$

$$\Gamma \quad = \quad GJ/EI = 2Gt/Et$$

where

E = modulus of elasticity of wall

G = shear modulus of wall

t = effective thickness of wall

Equations 4 and 5 were derived for isotropic shells. To apply these formulas to the problem of the filament-wound ring it is necessary to estimate the section properties EI, Et, Gt. For this purpose, a netting analysis was made assuming the wall to be a portion of a slender filament-wound cylinder of the same wall construction. The results of this analysis are:

$$\left. \begin{array}{rcl} EI & = & \frac{1}{2} n(EA)_H r^2 \mu \cos^3\theta_H \\[2mm] GJ & = & n(EA)_H r^2 \sin^2\theta_H \cos\theta_H \\[2mm] Gt & = & \frac{1}{2\pi r} n(EA)_H \sin^2\theta_H \cos\theta_H \end{array} \right\} \qquad (6)$$

7

where n = total number of helical fibers

$(EA)_H$ = stiffness of each helical fiber

θ_H = angle between helical fiber and equatorial direction (at mean radius).

μ = factor to account for compliance of meridional fibers

$$= \left[1 + \frac{(EA)_H}{(EA)_M} \sin^3 \theta \right]^{-1}$$

$(EA)_M$ = combined stiffness of meridional fibers associated with one triangular unit cell defined by the helical winding

The use of these formulas for buckling of a toroid implies the assumption that the loading on the toroid remains directed toward the axis as the deformation progresses. This is believed to be a realistic assumption for the aft ring of a tension-cone decelerator, since the load is applied through meridional fibers that lead toward the axis. It is perhaps worth noting in passing that for hydrostatic loading, for which the loading remains locally normal to the ring as the deformation progresses, the critical buckling loads for both cases are somewhat lower than those for the respective radial-loading cases.

Static Test Specimens

Toroids of two different geometries were used in the buckling tests. These toroids were constructed with Dacron fiber wound onto an elastomeric bladder which had been formed over a rigid wash-out mandrel. The windings were bonded together and to the bladder by painting with a thin solvent-solution of elastomeric resin.

The first test item, which is shown in Figure 4, was constructed with a closely spaced, machine-wound, meridional wrapping of Dacron roving, covered with a coarse-mesh, double helical wrapping which was hand-wound using braided Dacron tape. The toroid has an equatorial diameter of 20.8 inches and a meridional diameter of 2.5 inches, giving a "slenderness ratio", R_b/r equal to 8.3. The design burst pressure was 600 psi. Design data for this toroid are summarized in Table I.

The buckling loads for the toroid were estimated using equations 4 and 5. The section properties were calculated from equation 6 using measured properties of the filamentary materials with an effective helix angle as measured at the mean radius of the toroid cross section. The numerical values used for this calculation were n = 30, θ_H = 35°, $(EA)_H$ = 1500 lb, μ = 0.9, r = 1.26 in.

The calculated properties are then EI = 18 x 10^3 lb in^2, Γ= 1.09, $\bar{R}$ = 9.14 in, c = 0.138, S = 28.3, S + P* = 32. Note that S + P* depends on internal pressure, but is essentially constant for the pressure range of interest (0 to 200 psi).

If these quantities are substituted into the buckling relations, the results are as follows:

For inplane buckling (equation 4)

$$P_{cr} = 3.3 \frac{EI}{\bar{R}^2} = 710 \text{ lb}$$

For out-of-plane buckling (equation 5)

$$P_{cr} = 1.7 \frac{EI}{\bar{R}^2} = 370 \text{ lb}$$

The requirements for deployment under load and for aerodynamic stability for the deployable decelerator led to a toroid geometry which is somewhat less slender than the toroid described above. The "stout" toroid shown in Figure 5 was used in the designs for the deployable decelerator models.

The stout toroids had basically the same construction as the slender prototype toroid, with an elastomeric bladder and three layers of filament-wound structural fiber (one meridional layer and two opposing helical layers). One important difference in construction is that the helical layers on the stout toroids were relatively closely-spaced, uniformly-distributed windings made by machine, as opposed to the coarse, hand-wound net of braided tape on the slender prototype. A second difference is that the meridional layer was wound outside the helical layers, to assist in holding the helical windings in place. The equatorial diameter of the toroid shown in Figure 5 is 18 inches and the meridional diameter is 3.15 inches, giving R_b/r = 5.7. The toroid was designed to burst at a pressure of 250 psi with a sharp bend, assuming a bending stress factor of 3.0 (i.e., assuming that the maximum stress in the helical fibers in the bent section is three times the pressure-stress in the section before bending). Table I lists the design data for this toroid.

Since the decelerator was required to be packageable, it was important that the toroid wall be flexible. It was found that the toroid could be made adequately foldable by constructing the wall as a net of relatively heavy fibers, spaced several diameters apart and bonded together by painting with a light coating of solvent-dilute elastomeric resin. The open-mesh construction proved to be much less stiff than construction of the same strength using fine, closely-spaced fibers bonded together to form a more conventional composite shell.

TABLE I

DESIGN DATA FOR BUCKLING-TEST TOROID SPECIMENS

	Slender Toroid	Stout Toroid
General		
Outside diameter, inches	20.8	18.0
Meridional diameter, inches	2.52	3.15
Design burst pressure, psi	600	250 (bent)
Meridional Wrap		
Fiber	Dacron roving	Dacron roving
Fiber strength, lb	20	40
Wrap density at outer equator, turns/inch	40	10
Helical Wrap		
Fiber	Braided Dacron tape	Dacron roving
Fiber strength, lb	145	40
Wrap density at outer equator, each direction, turns/inch	1 (total 30 turns)	6
Wrap angle (measured from equator at mean radius)	35°	40°
Fiber stiffness EA, lb	1500	500

Test Apparatus and Procedure

The slender toroid was loaded in two different test fixtures, a "toggle-harness" arrangement and a double-cone vacuum bag, with essentially identical results over the range common to the two tests. The toggle harness, which is shown in Figure 6, consisted of an arrangement in which a double cone of "toggle strings" transformed an axial tension force into a radial load on the toroid through an array of radial strings. The load was applied by lengthening the cone with a hydraulic jack, and the axial force was measured with a mechanical force gage. The test runs were made with fixed internal pressure.

The toggle-harness arrangement had the disadvantage that the harness restricted the deformation by constraining all points on the inner equator of the toroid to lie a fixed distance from the rim of the toggle cone. This constraint prevented in-plane buckling. There was also some constraint against out-of-plane buckling, since the radial fibers tended to follow the out-of-plane deformation, instead of maintaining their original radial direction. Because of these difficulties, the toggle harness approach was abandoned in favor of a vacuum-bag loading apparatus.

The double-cone vacuum-bag setup is shown in Figure 7. This arrangement acts to load the toroid in a manner that is much more nearly like that expected from the aerodynamically loaded tension cone. The apparatus consists of a unidirectional-fabric bag which is gathered and held at both ends in structural clamps, the fabric bag being draped with a plastic-film bag which acts as a gas barrier. The structural fibers are bonded to the toroid at the center to form a double tension cone which loads the toroid radially in compression.

The axial force on the vacuum bag was measured with a mechanical force gage, and the vacuum in the bag was measured with a mercury manometer. The force on the toroid was computed from the axial force, the bag geometry, and the vacuum, taking into account the load contributions from the pressure difference acting on the cross-sectional areas of the evacuated structure.

The test procedure for the buckling tests on the slender toroid was as follows: The internal pressure of the toroid was set at some predetermined value, and then the axial load was increased by evacuating the bag until buckling occurred. For internal pressures of 100 psi or less, the toroid was pressurized with air. For higher pressures, the toroid was filled with water and connected to an air-filled accumulator tank in order to permit the buckling deformations to take place at essentially constant pressure.

The vacuum bag tests made on the stout toroids were concerned with both collapse and recovery from the collapsed condition, to simulate the loading which might occur during deployment. A total of three toroid configurations were tested in this way. The range of interest for internal pressure was zero to 25 psi, which corresponded to the range required for the deployment tests. As before, the internal pressure in the toroid was held constant and the load was applied by evacuating the bag.

Static Test Results and Discussion

The behavior of the slender toroid in the toggle-harness loading fixture was as follows: When the hoop force reached a value at which a compression wrinkle could develop, the toroid buckled in a mode shape consisting of two planar semicircles joined at "hinges" on a diameter, as shown in Figure 8. For the lower range of internal pressures, this wrinkling force was typically about 30 lb greater than the pressure load on the meridional cross section (i.e., $p\pi r^2$). At the higher pressures, where the compressive load could exceed the critical load for out-of-plane buckling, the toroid developed a small "curling" deformation, as shown in Figure 9. This deformation developed its full amplitude (about that shown in the figure) with a load increase of a few percent over that at which it started. The ability of the toroid to support additional load was not seriously impaired, however, since the load could be increased until the $p\pi r^2$ value was reached, at which time the deformation shown in Figure 8 would occur.

The load-carrying ability of the slender toroid in the vacuum-bag setup was essentially the same as that observed in the toggle-harness tests. At low internal pressure, the buckling load indicated that the toroid wall was supporting some compressive force. When the compressive force exceeded the predicted critical load for out-of-plane buckling, the toroid developed a small curling radius immediately and then ceased to grow as the load was increased. For higher internal pressures in the toroid, buckling failure continued to occur near the $p\pi r^2$ load until the critical load for the in-plane buckling mode was reached, beyond which point further increase in pressure produced no significant increase in load-carrying capability.

The experimental results of the vacuum bag tests on the slender toroid are shown by Figure 10. The plotted points show the calculated values of hoop force, as determined from measured values of peak axial force for each test. It can be seen from the figure that good agreement was found between the experimental results and the slender isotropic-shell theory for critical buckling loads in the two modes.

A photograph of the buckled slender toroid in the vacuum bag is shown in Figure 11. The shape of the completely collapsed toroid was usually a planar figure with four circular arcs and four "hinges", although there was occasionally some out-of-plane deformation. Figure 12 shows the development of the planar four-hinge collapse mode. For the low-pressure runs, the collapse deformation progressed slowly, with the axial force dropping rapidly at first and then more slowly. The higher-pressure runs, with the relatively high vacuum (as much as 20 inches of mercury), produced violent collapses, since there was considerable pressure differential on the bag, even after the toroid had collapsed completely. All of the collapse behavior observed had the nature of the catastrophic failure, however, since the axial force dropped rapidly as soon as the deformation produced an observable wrinkle.

One unexpected result of these tests was that the ring did not collapse in the out-of-plane buckling mode. It is assumed that the reason for this behavior is that the direction of the applied load follows the deformation in a way such that the effective bending-moment arm does not increase with deformation. It is believed, however, that the vacuum bag test simulates with reasonable accuracy the loading condition on a ring used as the base support for a tension-cone decelerator. To the extent that this is true, the implication of the test results is that the designing condition for the aft ring for a tension cone is the in-plane buckling mode rather than the out-of-plane mode. This means, in effect, that the optimum-design ring can be somewhat more slender and also somewhat lighter than a ring designed to prevent out-of-plane buckling.

The test results on the stout toroid are shown in Figures 13 and 14. Figure 13 shows the results obtained for two different toroids which were identical in every respect except for the flexibility of the wall. One had a heavy coating of matrix material, making the wall relatively stiff and hard to fold, while the other had a minimum amount of matrix material and was considerably easier to fold. The graph shows the peak hoop force, plotted against the internal pressure load on the cross section. The shaded areas define the envelopes of the test data. The shaded area above the $P = p\pi r^2$ line represents the collapse of the toroid under increasing load. The area below the line represents the peak force observed during recovery from the collapsed condition as air was re-admitted slowly into the vacuum bag. This peak force occurred during the final stage of the recovery. The load-carrying ability of the toroid under complete collapse was a small fraction of this value.

The considerable width of the shaded areas in Figures 13 and 14 is partly due to a small amount of experimental scatter, but is primarily the result of a "memory" effect by which the toroid collapses or recovers at progressively lower loads until a lower limit is reached. This effect is readily observed and understood for the collapse condition; the fact that the collapse occurs at a load higher than $p\pi r^2$ is due to the compression strength of the structural wall,

13

and the presence of an established wrinkle can be expected to decrease the resistance to "local crippling" at the wrinkle.

During the experiment it was found that the high buckling load could be reproduced readily by allowing the pressurized toroid to sit without load for perhaps a half hour, after which a repeat of the sequence of progressively lower collapse loads could be observed. The experimental spread of collapse loads was essentially constant for the entire range tested, which fact tends to support the conclusion that this effect results from the properties of the structural wall and is therefore independent of pressure. It can also be seen that the stiff toroid had a considerably greater load-carrying capability than the flexible toroid, and that the experimental spread on the collapse load was approximately the same for both toroids.

The behavior of the toroid under recovery conditions was less easily understood. The experimental spread here was proportional to pressure and covered the same range for both toroids. One possible explanation is that the creases and folds developed by the toroid and the vacuum bag during collapse tend to resist straightening because of the frictional resistance to sliding of the surface over itself. Such frictional resistance can be expected to be proportional to pressure. Furthermore, the peak recovery force for the first cycle of collapse and recovery was always greater than the peak force in succeeding cycles. It is believed that a major portion of this effect is due to the folding of the vacuum bag and the associated change of direction of the "meridional" tapes, resulting in a non-radial component of load which acts to oppose the unfolding of the toroids.

In order to study the effect of the radial ties which have been found necessary for the decelerator (as described earlier), the flexible toroid was braced with a center ring and radial ties and then subjected to the vacuum bag test. The results of this test series are shown in Figure 14. Comparison of these results with those of Figure 13 shows that the center bracing had a relatively small effect on the collapse load but that the peak force during recovery was increased.

Perhaps the most significant result of the use of center bracing is the manner in which the post-buckling behavior is changed. In contrast to the behavior of the unbraced toroid, the center-braced toroid collapsed in a shape such that the vacuum bag retained a large cross-sectional area in the neighborhood of the toroid. A photograph of the well-developed collapse shape is shown in Figure 15. After the initial collapse, as the deformation progressed, the axial force dropped relatively slowly to about sixty percent of the peak value, and then remained approximately constant as the vacuum load increased. During recovery, as air was admitted to the vacuum bag, the axial force first dropped to about half the peak

value and then increased slowly as the toroid expanded. It is believed that the relatively high load-carrying capability of the collapsed toroid, when constrained by the center tie strings, is an important factor in the ability of the toroid to deploy reliably under aerodynamic load.

LARGE-DEFORMATION FOLDING-HINGE MOMENT FOR AN INFLATED TUBE

The ability of an inflatable toroid to deploy under load depends on the "hinge moment" developed at the folds during the inflation process. This large-deformation bending resistance is not easily predicted theoretically because of the manner in which the cross-section shape varies with fold angle. In order to obtain the moment vs angle relationship required for the present study, an experiment was set up to make measurements on an inflatable tube. The test sample used was a cylinder of the same cross section and construction as that of the slender prototype toroid.

The experimental apparatus for the hinge-moment measurements is shown in Figure 16. The apparatus was designed to simulate the loading conditions for the hinges of a folded toroid expanding against a radial compressive load. Thus, the hinge was loaded both in compression and in bending by a compressive load which was applied in a direction normal to the plane of symmetry of the hinge. In addition, the hinge was placed at the center of a long tube in order that the section near the hinge would not be influenced by end effects. The cable tension required to equilibrate the hinge moment was measured for each five degrees of fold half-angle from 10 to 85 degrees. Because of the large forces which would have been required, no measurements were made at angles less than ten degrees. Three values of internal pressure (30, 50, and 70 psi) were used. The hinge moment for each angle was determined from the cable tension and the offset of the cable from the hinge.

The reduced experimental results are shown in Figure 17. There was no systematic difference in the results obtained for the various values of internal pressure. As shown in the figure, the hinge moment is essentially constant at

$$M_{hinge} = 0.55 \ p\pi r^3 \qquad\qquad (7)$$

over the range from 10 to 55 degrees of fold half-angle. For greater fold angles, the interference on the compressive side of the fold begins to increase rapidly, thereby increasing the stiffness through a rapidly increasing cross-section moment of inertia.

ANALYSIS OF DEPLOYMENT MECHANICS

It is of interest to develop an analytical model for the process of deployment of an inflatable tension-cone decelerator in order that

some insight may be gained into the principal characteristics of the process. Because of the great complexity of the problem, it is obviously not possible to represent the deployment process accurately. It is possible, however, by making a number of reasonable assumptions, to simplify the problem enough to be able to uncover some details concerning the essentials of the deployment behavior.

In the analysis which follows, the problem has been reduced to one of static equilibrium of the toroid. The assumptions concerning the shapes of the toroid and tension cone are based on observations of models under static loads and in subsonic deployment tests. The model which will be considered here is shown in Figure 18. The toroid is assumed to be a thin ring which is folded forward, out of the plane, at two opposed hinges, forming two rigid semicircles connected on the diameter. It is assumed that the forces on the toroid from the taut tension cone are such that the lines of action all pass through a single point on the axis of the cone. This model is a reasonably accurate representation of the observed geometry. It permits a straightforward calculation of the bending moment as a function of hinge angle if an assumption is made for the tension distribution around the ring. For the present analysis, the tension distribution will be taken to be uniform.

From Figure 18 it can be seen that the bending moment on each hinge is given by

$$M = \frac{1}{2} Fh \qquad (8)$$

where h is the height above the hinge axis of the line of action of the resultant force on one-half of the toroid, F . The height h can be computed from the condition that the net axial force on the toroid must be zero. Thus,

$$F_z = \int_0^\pi T_z' R d\phi = 0 \qquad (9)$$

where

$$T_z' = T' \cos\psi$$

and T' is the uniform cone tension per unit length of ring circumference. Substituting for T_z' and dividing by the constant

factors R and T', the integral of equation (9) which must vanish, is seen to be

$$\int_0^{\pi/2} \cos\psi \, d\phi = 0 \qquad (10)$$

From Figure 18, it can be seen that

$$\tan\psi = \frac{R\cos\varepsilon}{h - R\sin\varepsilon} \tag{11}$$

and

$$\sin\varepsilon = \sin\phi\,\sin\theta \tag{12}$$

Using these relations, it is possible to express equation (10) in the form

$$\int_0^{\pi/2} \frac{(\eta - \sin\phi\,\sin\theta)d\phi}{[1 + \eta^2 - 2\eta\,\sin\phi\,\sin\theta]^{\frac{1}{2}}} = 0 \tag{13}$$

where $\eta \equiv h/R$.

Equation (13) is an integral equation for the unknown quantity η . This equation has been solved numerically and the solution is plotted in Figure 19. It is possible to obtain an approximate analytical solution to this equation by neglecting the term $2\eta\,\sin\phi\,\sin\theta$. The result is

$$h/R \equiv \eta \simeq \frac{2}{\pi}\sin\theta \tag{14}$$

This result is accurate for small θ and reasonable for $\theta < 60°$. It is shown in Figure 19 compared with the numerical solution.

The resultant force F may be computed from the relation

$$F = 2\int_0^{\pi/2} T'R\,\sin\psi\,\sin\beta\,d\phi \tag{15}$$

which can be verified by inspection of Figure 18. After some manipulation

$$\sin\psi = \frac{\cos\varepsilon}{[1 + \eta^2 - 2\eta\,\sin\theta\,\sin\phi]^{\frac{1}{2}}} \tag{16}$$

and

$$\sin\beta = \frac{\sin\phi\,\cos\phi}{\cos\varepsilon} \tag{17}$$

17

Substitution of these relations into equation (15) gives an expression for F in terms of θ

$$F = 2T'R \cos\theta \int_{0}^{\pi/2} \frac{\sin\phi \ d\phi}{[1 + \eta^2 - 2\eta \sin\theta \sin\phi]^{\frac{1}{2}}} \quad (18)$$

This expression for F is evaluated and plotted in Figure 20 as F/2T'R .

The bending moment on the hinge is given by equation (8) combined with the results of equations (13) and (18):

$$M = \frac{1}{2} Fh = \left(\frac{h}{R}\right) \left(\frac{F}{2T'R}\right) T'R^2 \quad (19)$$

The quantity $T' \equiv nT/2\pi R$ can be determined from equation (1) by noting that the base area is $\pi R^2 \cos\theta$. Thus

$$T'R^2 = \frac{C_D^* q R^3 \cos\theta}{2 \cos\alpha_h} \quad (20)$$

where C_D^* is the drag coefficient of the folded configuration. After substituting this expression into equation (19) it is possible to express the bending moment in the following non-dimensional form:

$$\frac{M}{q\pi R^3} = \left(\frac{h}{R}\right) \left(\frac{F}{2T'R}\right) \frac{C_D^* \cos\theta}{2\pi \cos\alpha_h} \quad (21)$$

The non-dimensional bending moment is plotted in Figure 21. The maximum value of this function occurs at about θ = 40° and has the value

$$M_{max} = 0.045 \ q\pi R^3 C_D^*/\cos\alpha_h \quad (22)$$

It has been shown (Figure 17) that the restoring moment developed at a folding hinge is essentially constant over the range of θ from 10 to 55 degrees and has the value given by equation (7). Since the applied moment has a maximum value (near θ = 40°), the critical conditions for deployment will occur at the point of maximum applied moment. One condition for deployment can therefore be obtained by requiring that the restoring hinge moment from equation (7) be greater than the maximum applied bending moment from equation (22). This condition reduces to the inequality

$$\frac{p}{q}\left(\frac{r}{R}\right)^3 \frac{\cos\alpha_h}{C_D^*} \geq 0.082 \qquad (23)$$

which insures that the toroid will not fail to deploy because of lack of restoring moment at large fold angles.

A second condition for deployment is that the toroid must have enough hoop-force capability to straighten itself against the radial load in the final stages of the deployment. As described previously, this condition was examined experimentally using the vacuum-bag loading apparatus, with results as shown in Figures 13 and 14. Assuming that the toroid has the back-side center bracing and that this bracing becomes effective during the final portion of the deployment, the deployment condition is that

$$kp\pi r^2 > \frac{qC_D R^2}{\cos\alpha_h} \qquad (24)$$

where k is the factor by which the hoop force during the recovery is reduced below the nominal value of $p\pi r^2$. In non-dimensional form, this condition becomes

$$\frac{p}{q}\left(\frac{r}{R}\right)^2 \frac{k\cos\alpha_h}{C_D} \geq \frac{1}{\pi} \qquad (25)$$

It will be seen that both of the deployment conditions (23) and (25) contain, for given values of q and R , two free parameters (p and r) which characterize the toroid design. By taking the two conditions simultaneously to eliminate one of these parameters, it is possible to define a "best" toroid geometry, that is, a toroid geometry which will permit the same safety margin for both conditions. Thus, dividing (23) by (25) (assuming the equality in both cases) produces the "slenderness ratio"

$$\frac{r}{R} = .082\pi k \frac{C_D^*}{C_D} \qquad (26)$$

where it is assumed that $\cos\alpha_h$ is the same for both conditions.

For a numerical example, take $C_D = 1.3$, $C_D^* = 1.0$, k = 0.85. Then r/R = 0.17. By way of comparison, for the "stout" toroid which was tested, r/R = 1.57/9.0 = 0.175. Thus, the stout toroid geometry is near optimum for the example worked, under the various assumptions

19

which have been made. For the decelerator geometry of Figure 1, assuming $C_D = 1.3$, equation (25) gives the ratio $p/q \geq 18$.

UNDERWATER DEPLOYMENT TESTS

In order to study the deployment process under loading conditions which more nearly simulated the loading on an aerodynamic decelerator, a series of deployment tests were made in which an inflatable model was deployed and towed underwater. The specific objectives of these tests were to study the deployment and collapse of the model under the hydrodynamic load distribution and to develop deployment techniques which would be useful for later aerodynamic testing at high speeds.

Test Apparatus and Procedure

The design of the decelerator model is shown in the diagram of Figure 1 and in the photographs of Figure 22. The model was designed for a dynamic pressure of 300 lb/ft^2, or about 18 ft/sec in water. The flexible cone was constructed by bonding a meridional array of load-carrying fibers to a cloth surface, using an elastomeric matrix material. The cloth surface of the cone was formed from bias-cut gores which were bonded together with lap joints. The meridional strings were spaced about 0.3 inch apart at the base. The decelerator model used the previously-described stout toroid which consisted of three layers of structural fiber wound onto an elastomeric bladder.

The test apparatus used in the deployment tests included a forebody which was mounted on a sting as shown in Figure 23. The decelerator was packaged using a folding jig to insure reproducibility of the stowed configuration. The packaged decelerator was stowed in the aft end of the forebody and could be ejected at any desired time by a pneumatic piston which was held and released by a solenoid-operated trigger. The diameter of the stowed configuration was 7.5 inches. The frontal area of the stowed model was therefore 17 percent of the base area of the decelerator.

The inflation gas for the toroid was stored in a spherical container in the decelerator. A solenoid-operated valve was used to admit the gas to the toroid. The electrical signal to open the valve occured when a microswitch was actuated in the forebody, at the end of the ejection stroke. The component weights of the test decelerator are given in Table II.

The tow tests were conducted at the towing tank facility of Electric Boat Division of General Dynamics in San Diego. The tank is 6 feet deep and 12 feet wide. The decelerator model was suspended from the towing carriage so as to be centered in the tank cross section. Drag measurements were made with strain gages mounted on

TABLE II

COMPONENT WEIGHT OF WATER-TEST
MODEL DEPLOYABLE TENSION CONE DECELERATOR

Toroid	545 gm
Tension Cone	175 gm
Sphere	390 gm
Solenoid Valve	550 gm
Cable and Nose Piece	236 gm
TOTAL	1,796 gm

the sting and velocity was measured by tachometer and by a distance increment indicator. The data were recorded using a strip-chart recorder mounted on the carriage.

For the deployment tests, the decelerator model was initially packaged in the forebody with a preset pressure in the spherical gas storage bottle. After the carriage had been accelerated to the desired speed, at a predetermined station on the track, the ejection and deployment sequence was initiated. The decelerator was observed visually during these runs to determine whether deployment was complete.

In addition to the deployment tests, a series of collapse tests were made in order to measure the dynamic pressure required to collapse the toroid. In these tests the decelerator was initially deployed, with a given pressure in the toroid. The carriage was accelerated to a predetermined velocity and the shape of the ring was observed at that velocity.

Results and Discussion

The deployable decelerator model was found to behave essentially as expected except for a strong tendency to develop large fluctuations in the drag force. As a result, the drag-vs-velocity data were inconclusive. The recorded drag force oscillated steadily with an amplitude of about ten percent and a frequency of about three to four cycles per second. There was also a fluctuation in the local mean value of the drag force that gave a twenty percent variation in the computed drag coefficient. The average value of drag coefficient was about $C_D = 1.0$. The model had considerable lateral motion, and there was considerable "elastic" motion, in the way of pitching and "pumping" of the aft ring of the decelerator. Motion pictures showed that the meridional shape of the cone, as fabricated, was not correct for this type of low subsonic operation, since the surface wrinkled badly under the towing load.

The "steady-state" drag variation was found to be greater than the change in drag due to changes in velocity or decelerator geometry. It can be seen, however, that no large reduction in drag is possible with the given decelerator geometry, since the frontal area of the toroid is almost sixty percent of the decelerator frontal area. It was therefore not possible, from the drag force record, to ascertain when collapse occurred or when deployment was complete. For this reason, the indication of complete deployment was obtained visually.

The results of the underwater deployment tests are shown in Figure 24. The theoretical curve was based on the hoop-load condition, equation (25), assuming $\cos\alpha_h = 1.0$, $k = 0.85$, and $C_D = 1.0$. Equation (23), for the hinge-moment condition, gives

the same curve if it is assumed that $C_D^* = 0.8$. The tests showed that the decelerator had greater capability to deploy than the theory would predict. There is some evidence that the visual observations of deployment behavior may not have been entirely accurate since photographs showed small buckling deformations on some runs in which the toroid would probably have been judged to be fully deployed.

The shape taken by the toroid when deployment was incomplete was usually basically the same as that observed in the vacuum tests for the center-braced toroid (see Figure 15), except that there were often as many as four offsets in the buckled shape while there was never more than one offset in the vacuum tests. The two-hinge out-of-plane folding mode was not observed during the water tests.

Because of the lack of any distinct collapse mode (such as the two-hinge fold) for which the drag would change appreciably, the collapse tests did not yield useful quantitative data. The behavior of the model during these tests was such that buckling would develop gradually as the towing speed was increased, with the result that the frontal area was reduced very gradually. In the presence of the large oscillations in drag and in the absence of any adequate means for observing the model, there was no way to identify the point at which the compression-wrinkles started. However, it is important to note that, in collapsing, the decelerator did not drop the load catastrophically.

Since the two-hinge folding mode was not observed during these tests, it may be concluded that the toroid had more than enough hinge-moment capability to satisfy the large-fold-angle requirements for deployment. Furthermore, since the toroid geometry is close to that which satisfies both equation (23) (for hinge-moment capability) and equation (25) (for hoop-force capability), it appears that equation (23) is somewhat over-conservative.

The water tests demonstrated that an inflatable tension-cone decelerator can be made to deploy reliably from a small package under conditions of high dynamic pressure and low velocity. The decelerator performance, (in terms of the ratio of internal pressure to dynamic pressure) was considerably better than that which would be predicted by the elementary theory used in the design of the model; as shown in Figure 24, the decelerator was able to deploy and to develop the full drag force when the internal pressure was more than about sixty percent of the theoretically required value. It can be expected that similar results will be observed in deployment under high-speed conditions if flutter instability does not interfere.

CONCLUDING REMARKS

It has been demonstrated that an inflatable tension-cone decelerator can be made to deploy reliably from a small package under conditions of high dynamic pressure and low velocity. It has also been demonstrated that the performance of the decelerator can be predicted on the basis of elementary theory and static testing. The behavior of the inflated toroid used as the compression-resistant structure to support the base of the cone has been found to be predictable and essentially the same for both static loading and hydrodynamic loading on the tension cone. It has also been found that a filament-wound toroid can be made structurally efficient, adequately foldable, and highly resistant to damage from deployment and collapse under load. It is believed that the feasibility of this decelerator configuration has been adequately demonstrated in so far as the static-loading and deployment aspects are concerned.

Astro Research Corporation
    Santa Barbara, California, October 26, 1966.

REFERENCES

1. Roberts, L.: Entry Into Planetary Atmospheres. Astronaut. Aeron., vol. 2, no. 10, Oct. 1964, pp. 22-29.

2. Anderson, Roger A.: Structures Technology - 1964. Astronaut. Aeron., vol. 2, no. 12, Dec. 1964, pp. 14-20.

3. MacNeal, Richard H.: Flutter of Towed Rigid Decelerators. NASA CR-766, 1967.

4. MacNeal, Richard H.: The Flutter of Flexible, Towed Tension Shells. NASA CR-777, 1967.

5. Anderson, M. S.; Robinson, J. C.; Bush, H. G.; and Fralich, R. W.: A Tension Shell Structure For Application to Entry Vehicles. NASA TN D-2675, 1965.

6. Timoshenko, S.: Strength of Materials, Part II. Third Ed., D. Van Nostrand, Inc., 1956.

7. Weeks, George E.: Buckling of a Pressurized Toroidal Ring Under Uniform External Loading. NASA TN D-4124, 1967.
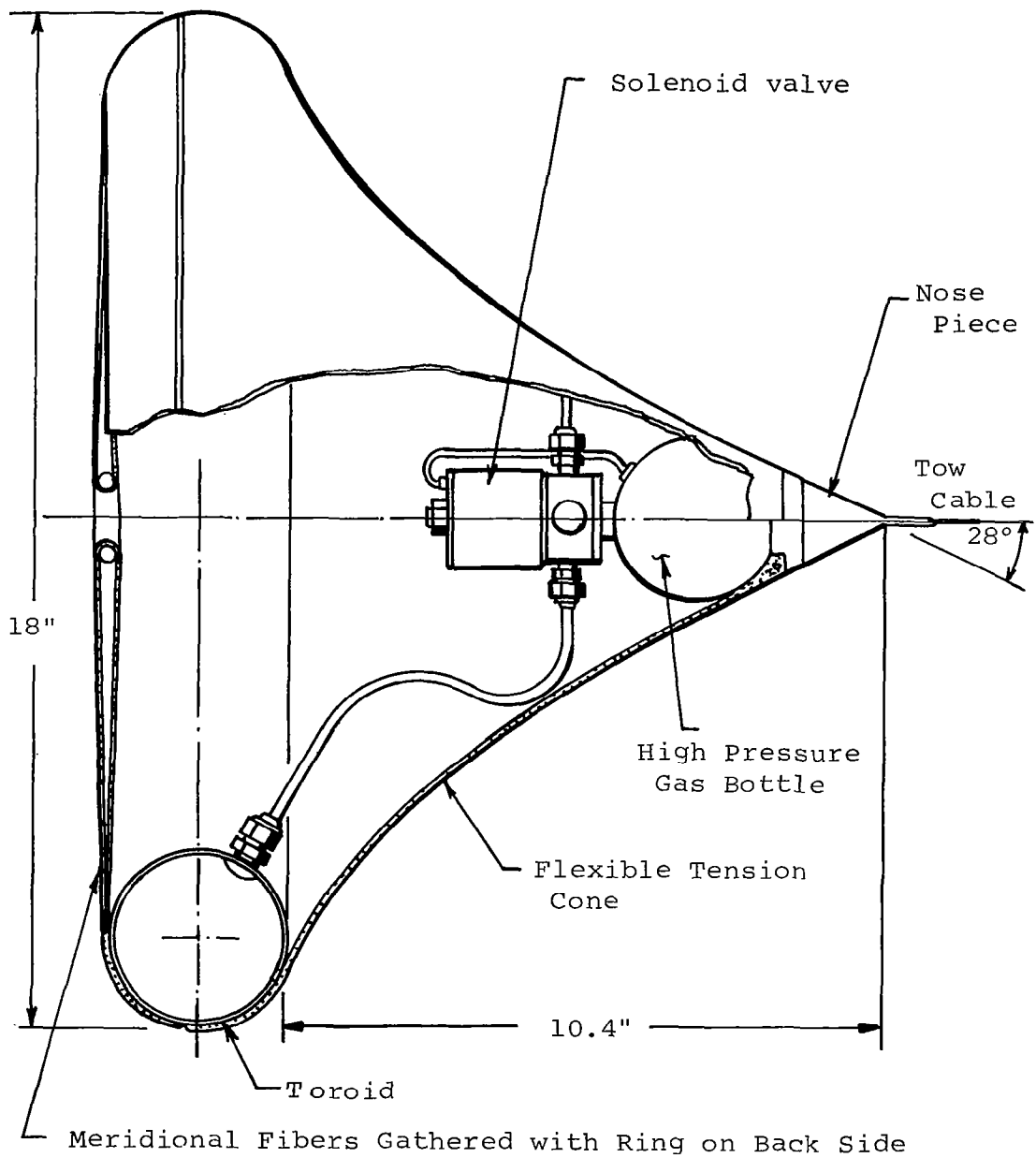
Figure 1. — Decelerator Configuration

The following labels appear in the figure:

- Solenoid valve
- Nose Piece
- Tow Cable
- 28°
- 18"
- High Pressure Gas Bottle
- Flexible Tension Cone
- 10.4"
- Toroid
- Meridional Fibers Gathered with Ring on Back Side
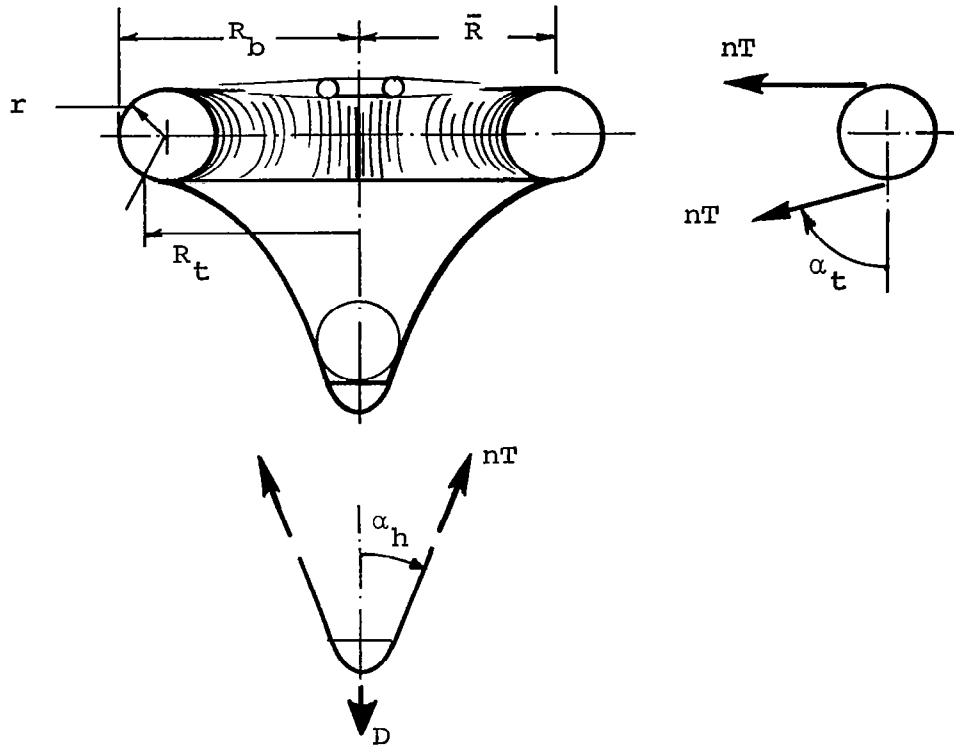
Figure 2. — Coordinates and Loads on Elements of Decelerator

(a) Meridional Fibers
    Bonded to Toroid

(b) Meridional Fibers Looped
    Around Toroid
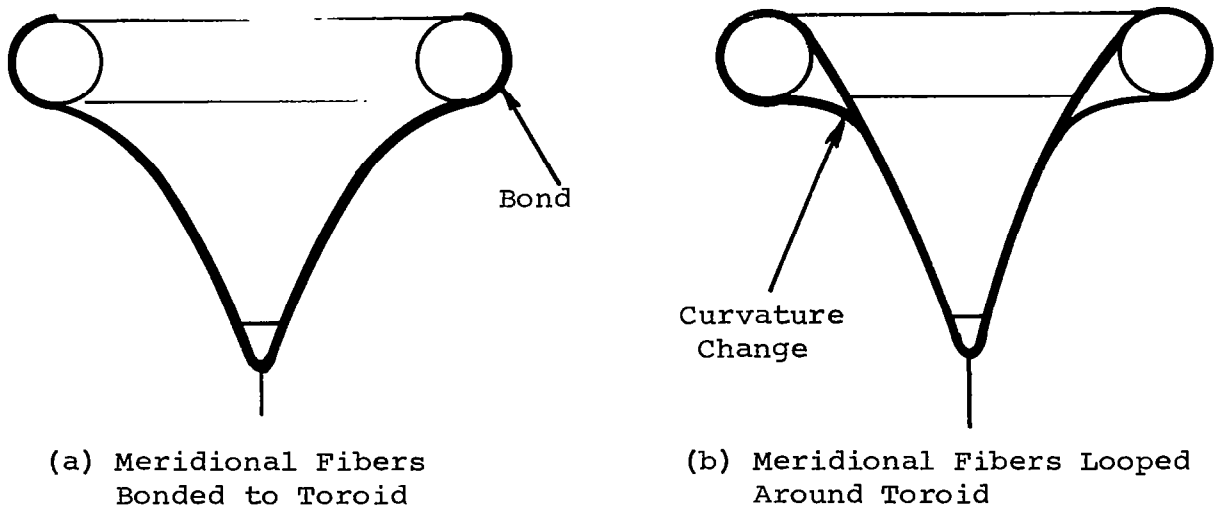
Figure 3. — Alternative Methods of Attaching Cone to Toroid
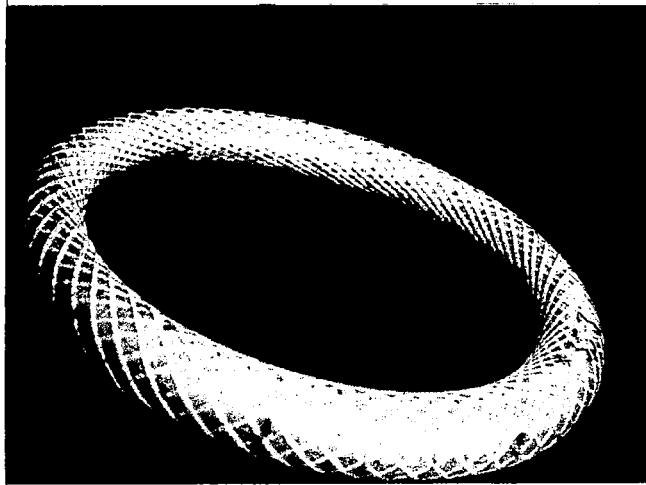
Figure 4. __ Slender Prototype Toroid
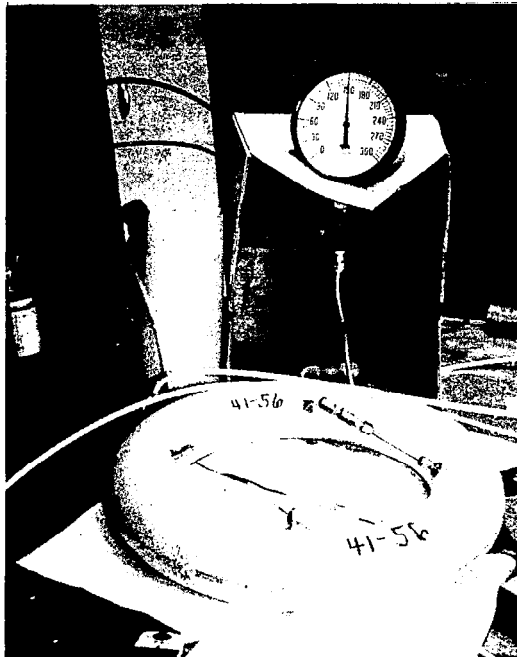
Figure 5. — Stout Toroid
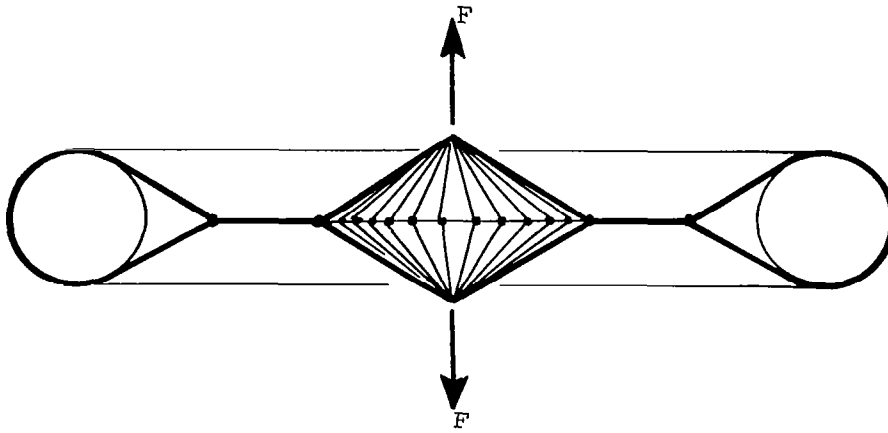
Figure 6. — Toggle-Harness Apparatus for
Radial Compression Tests
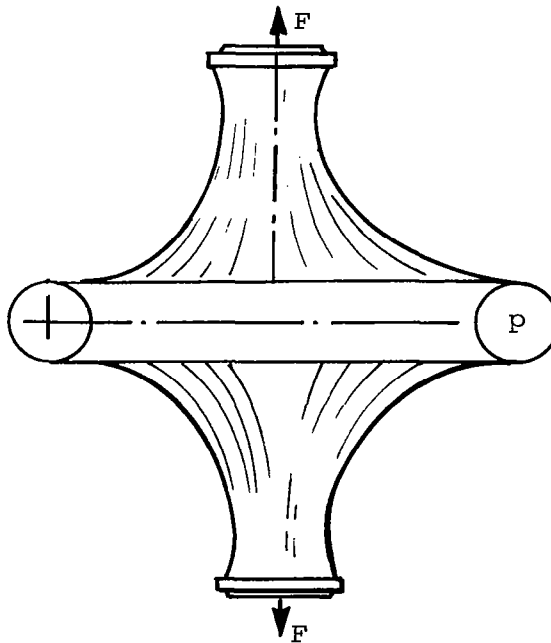
Figure 7. — Vacuum-Bag Apparatus for Compression Tests
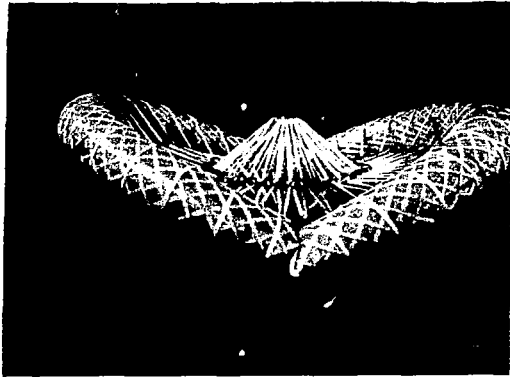
Figure 8. — Compression-Wrinkle Collapse of Slender Toroid in Toggle Harness
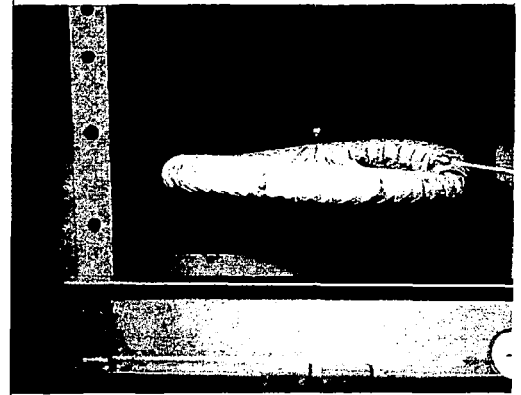
Figure 9. — Out-of-Plane (Curling) Deformation of Slender Toroid in Toggle Harness
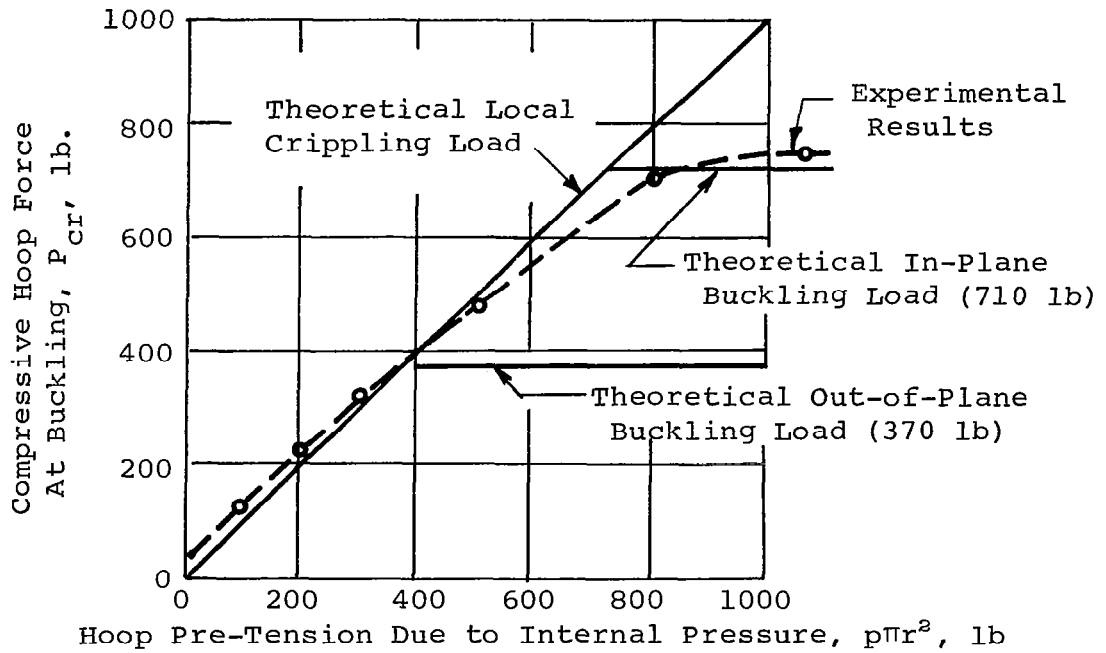
Figure 10. — Experimental Results For Vacuum-Bag Tests On Slender Toroid

Figure 11. — Collapsed Slender Toroid in Vacuum Bag
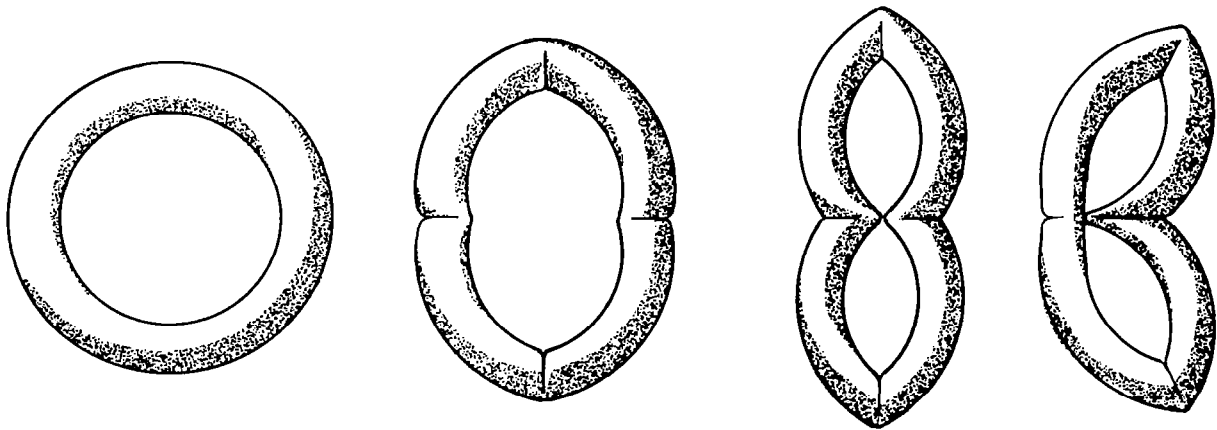
Figure 12. — Development of Four-Hinge
Planar Collapse Mode

31
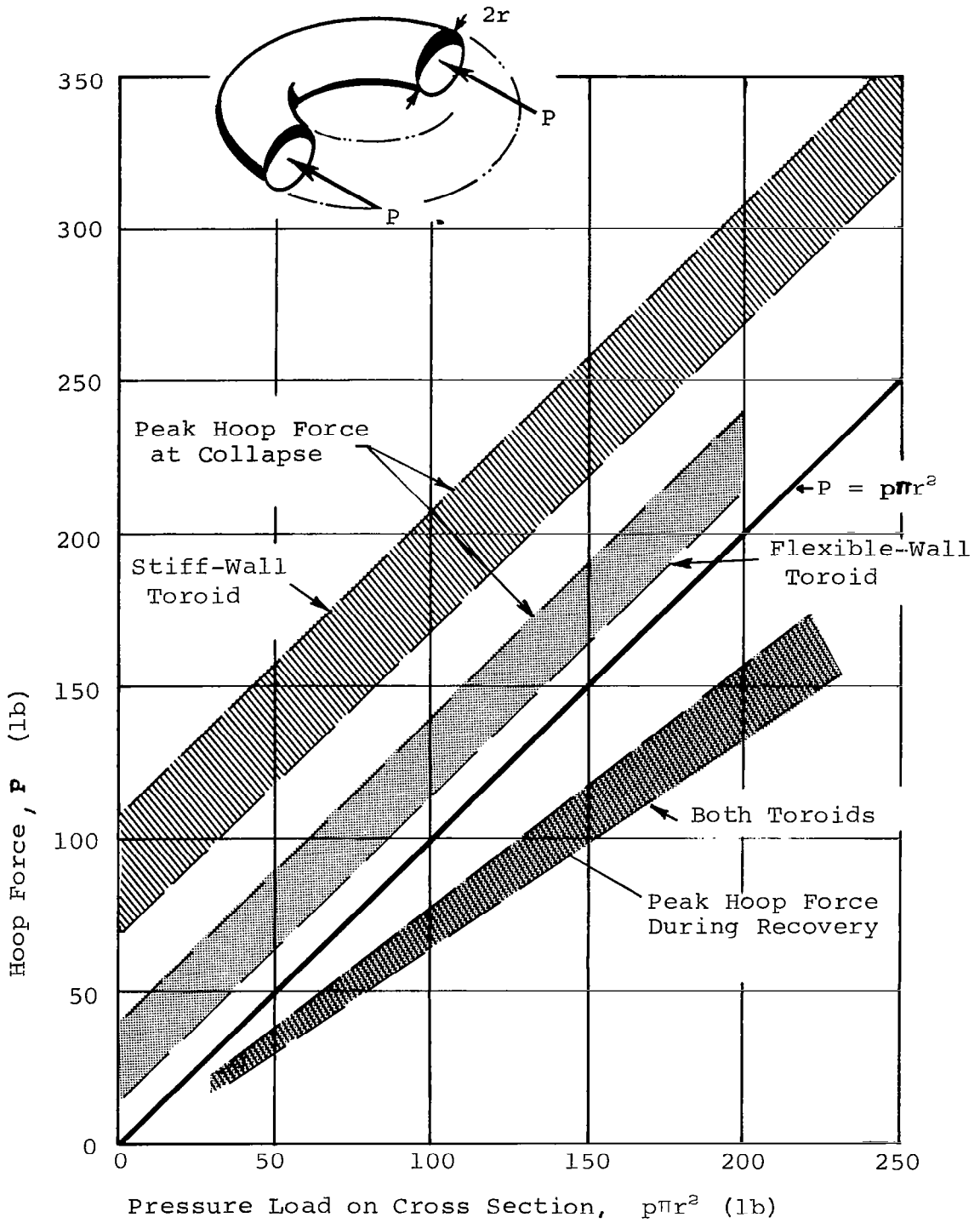
Figure 13. — Experimental Results For Vacuum-Bag
Tests on Stout Toroids Without Center Bracing
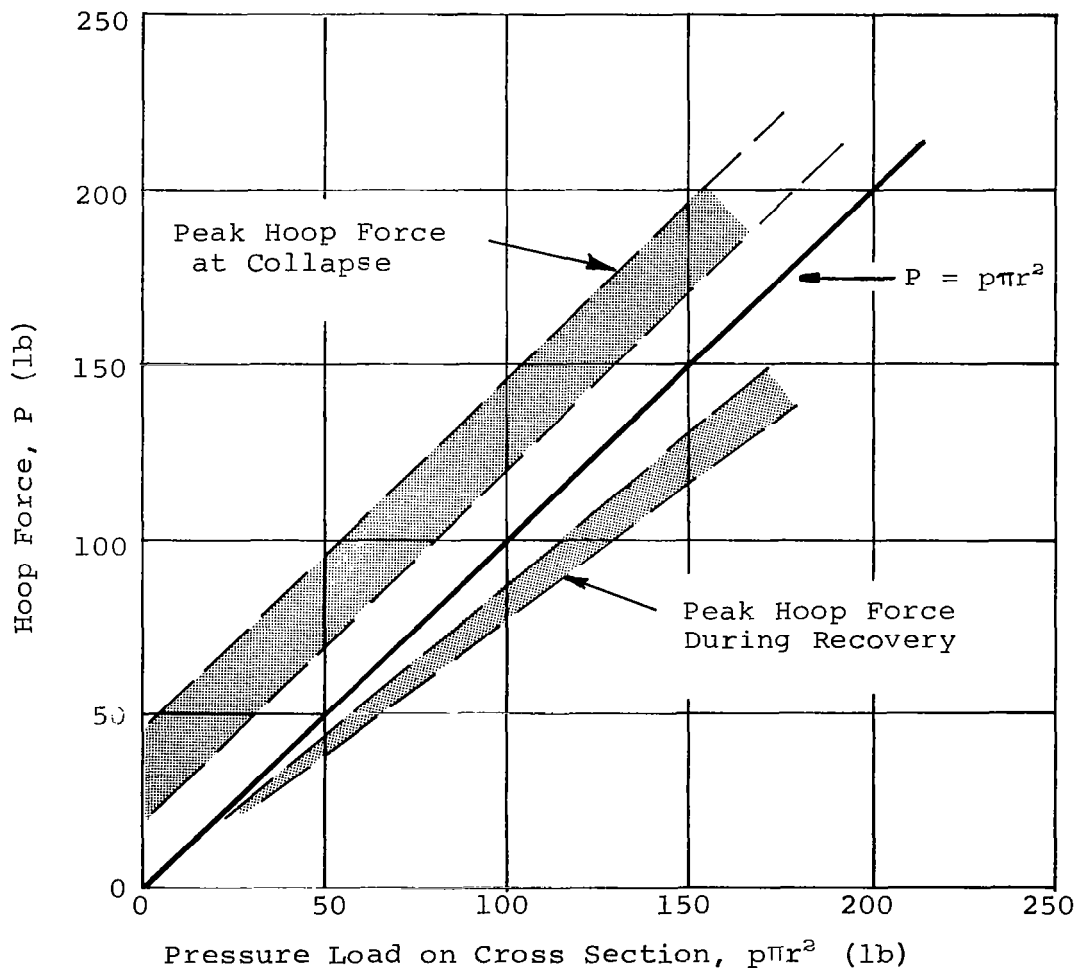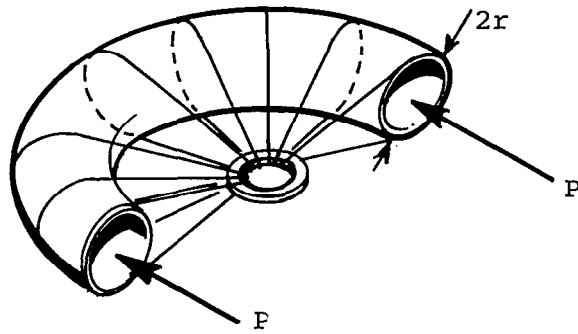
Figure 14. — Experimental Results For Vacuum-Bag Tests
On a Stout Toroid With Center Bracing

Figure 15.   Collapse Shape for Stout
              Toroid With Center Ties
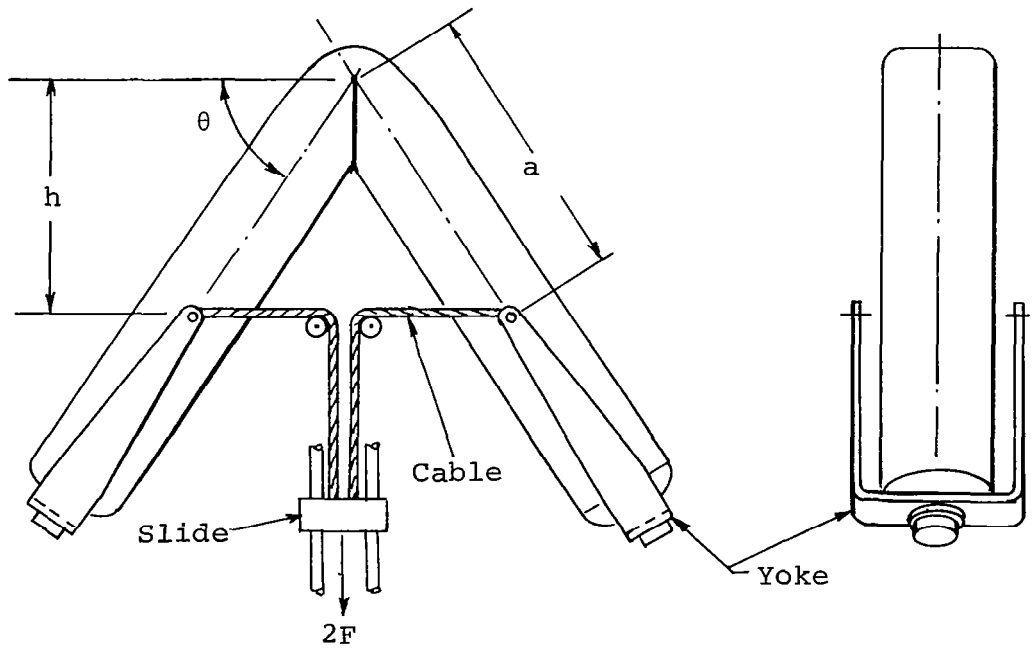
Figure 16. — Cylinder Test Fixture
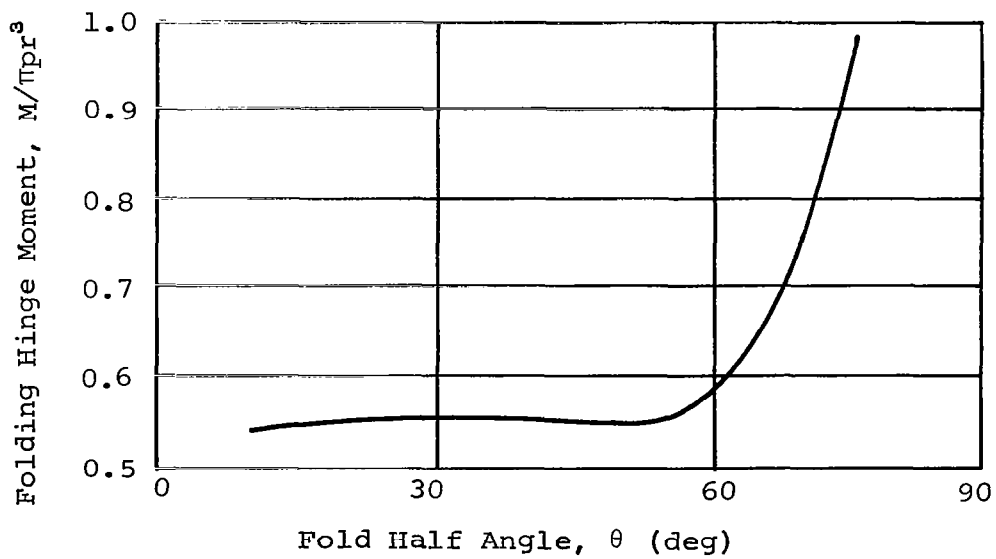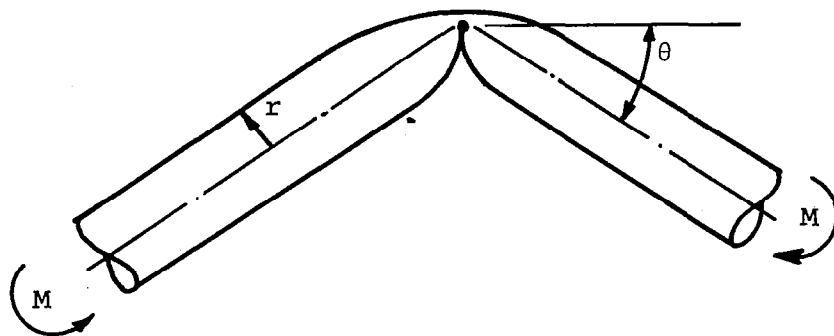
Figure 17. — Folding Hinge Moment for an
Inflated Tube
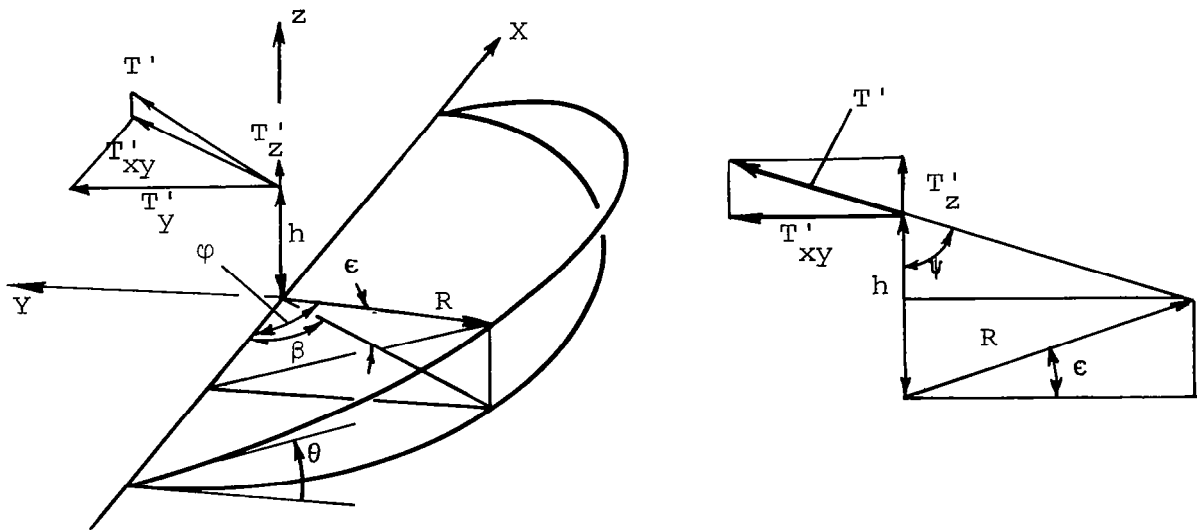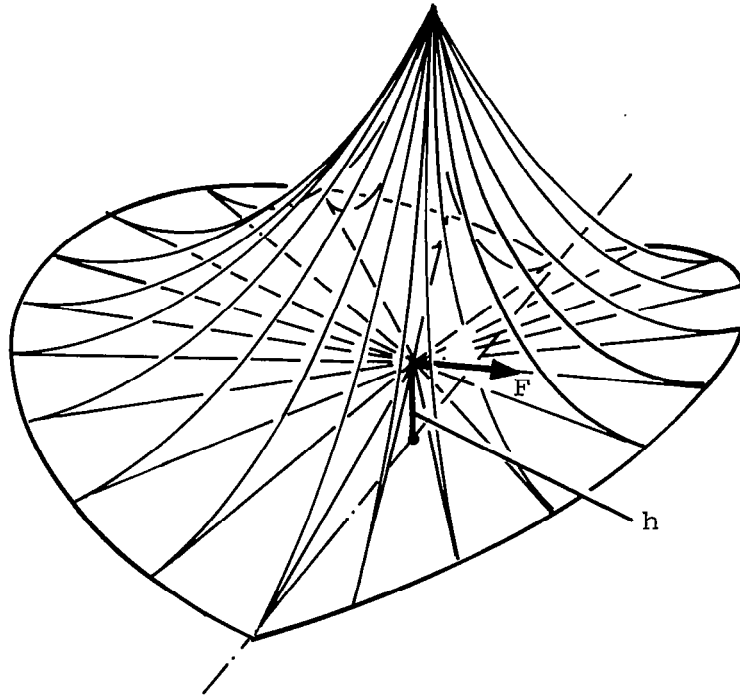
Figure 18. — Model For Deployment Analysis
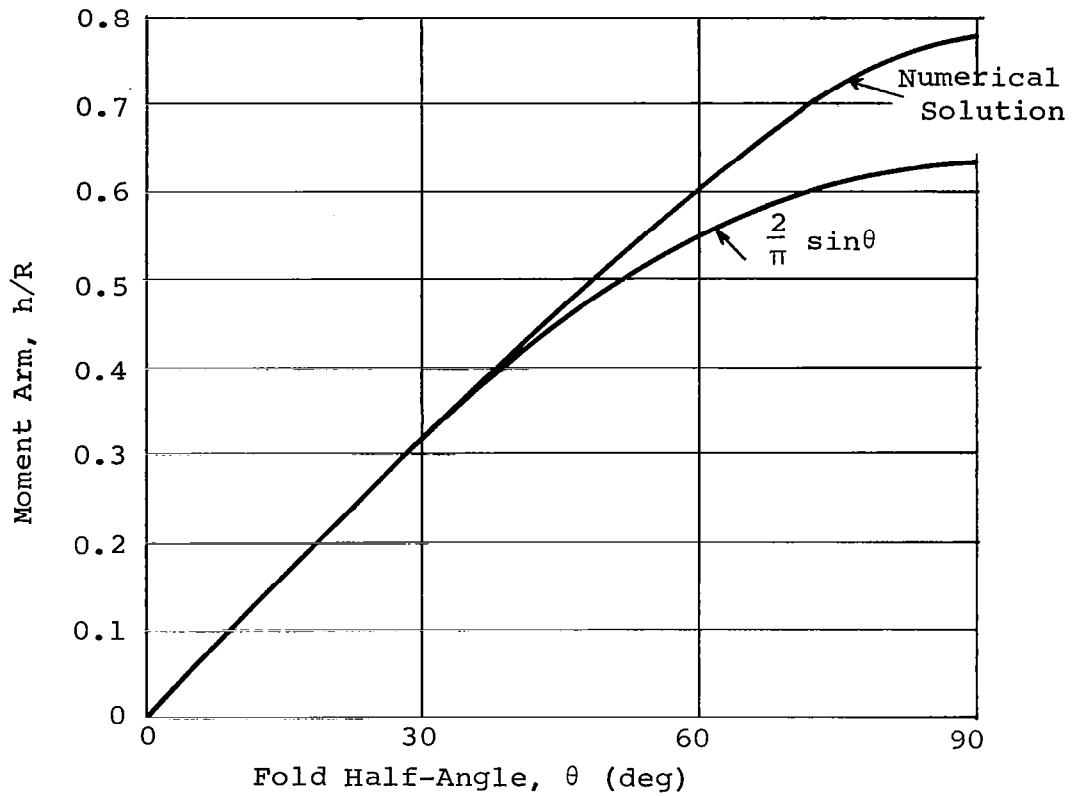
Figure 19. — Solution of Equation (13)
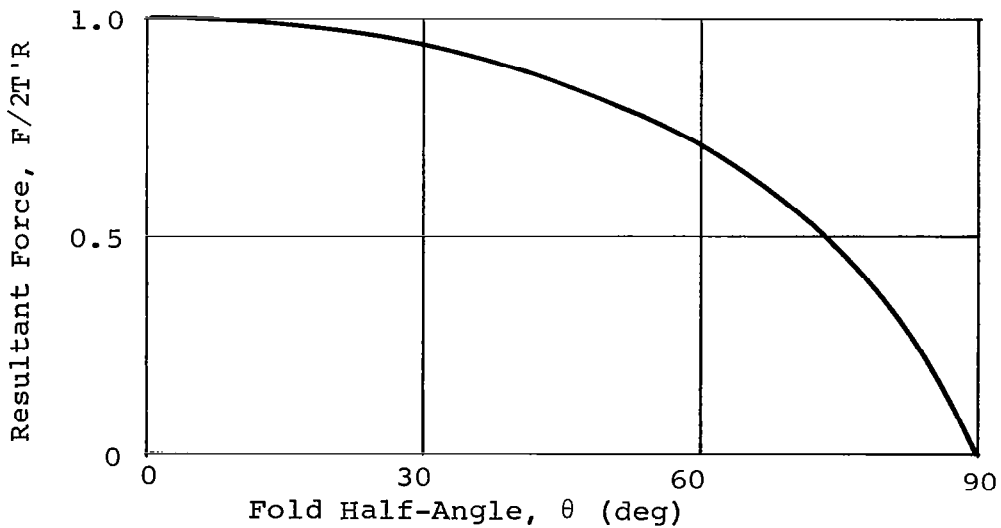
Figure 20. — Resultant Force on Half-Toroid

37
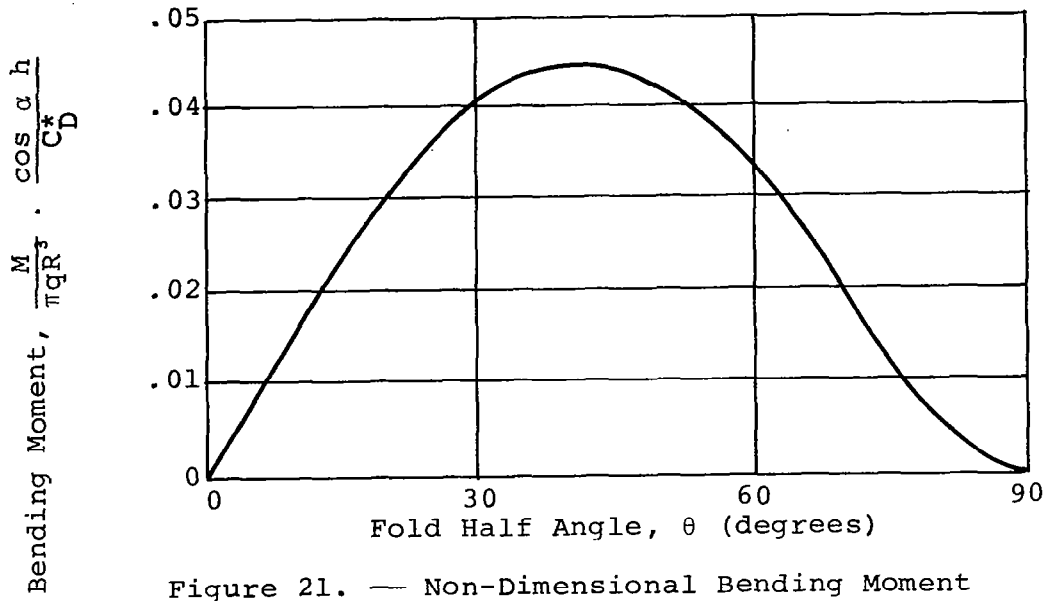
Figure 21. — Non-Dimensional Bending Moment
of Collapsed Toroid
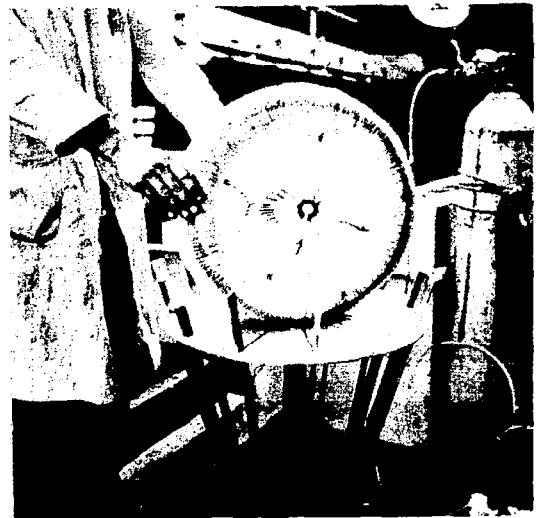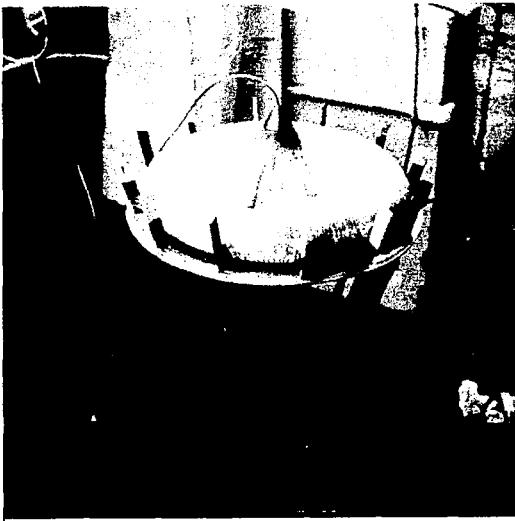
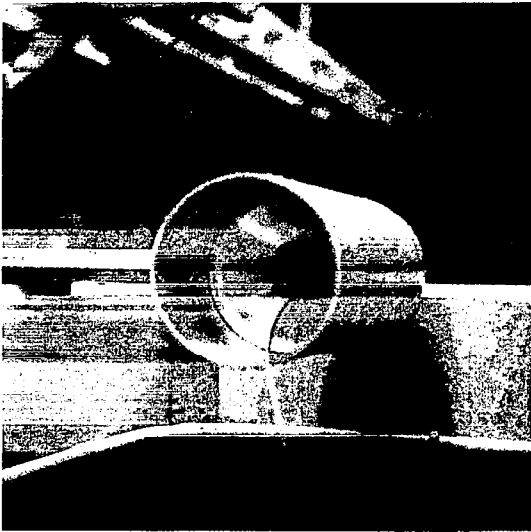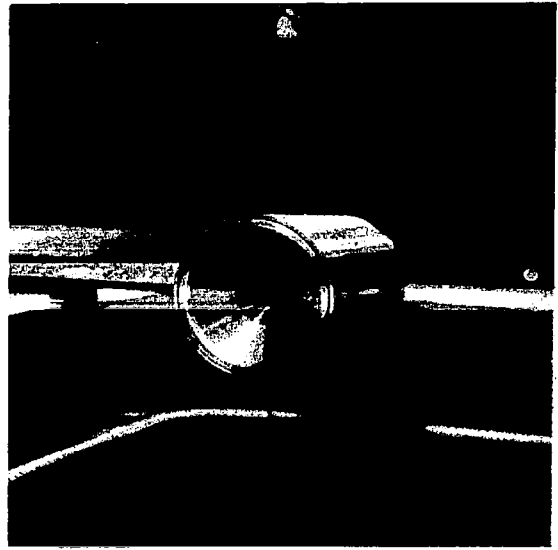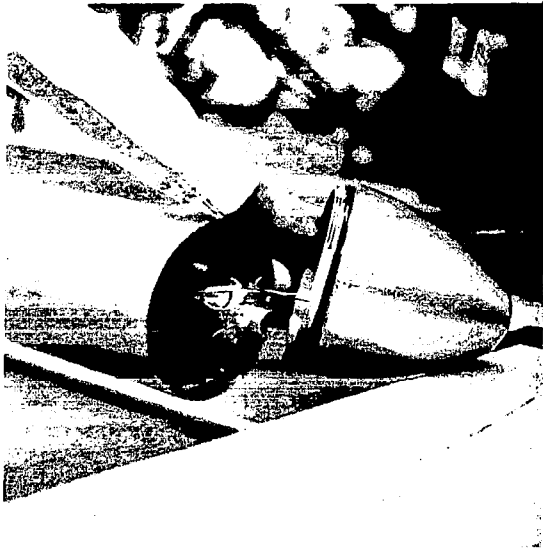Figure 22. — Decelerator Model for
Underwater Testing
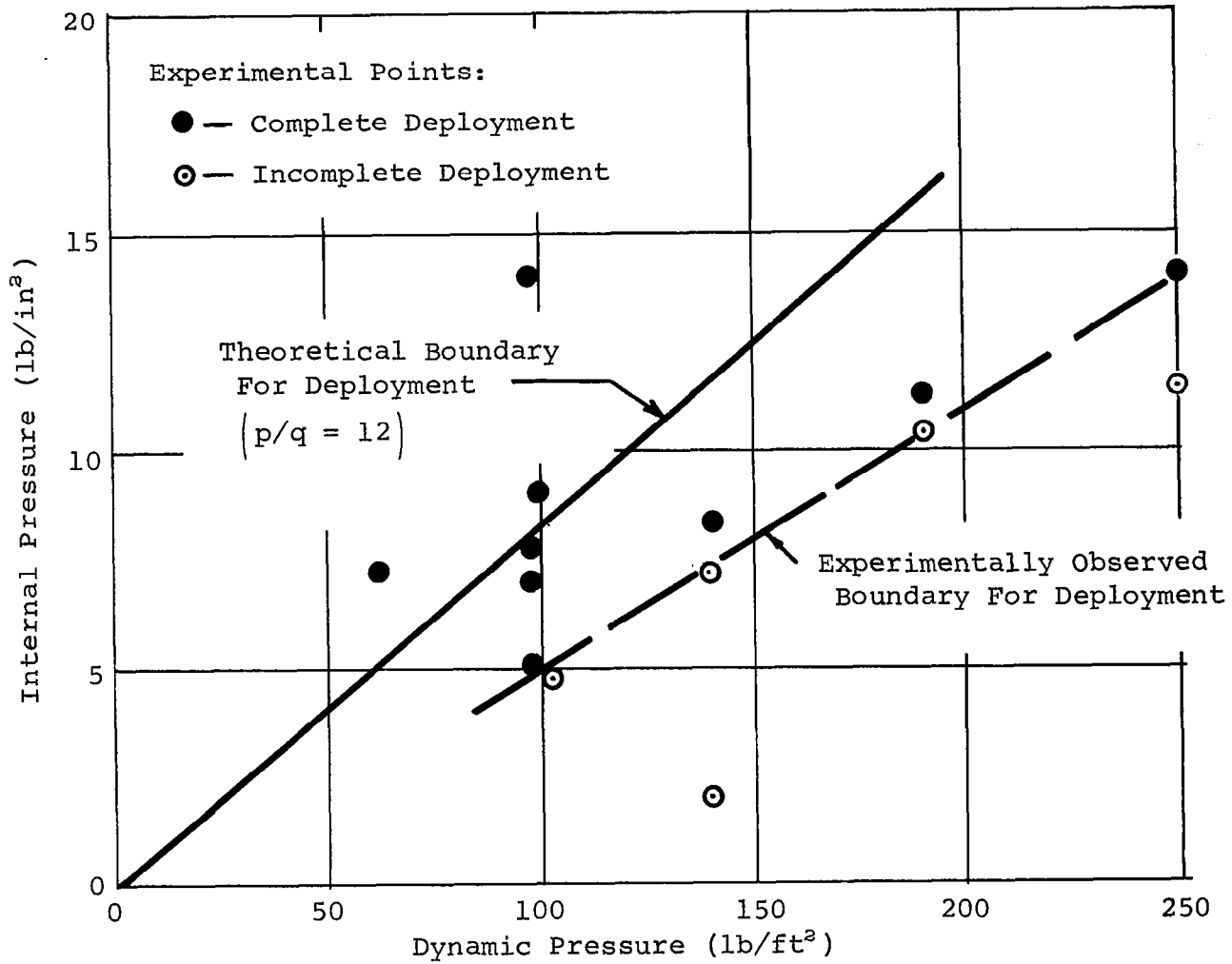
38
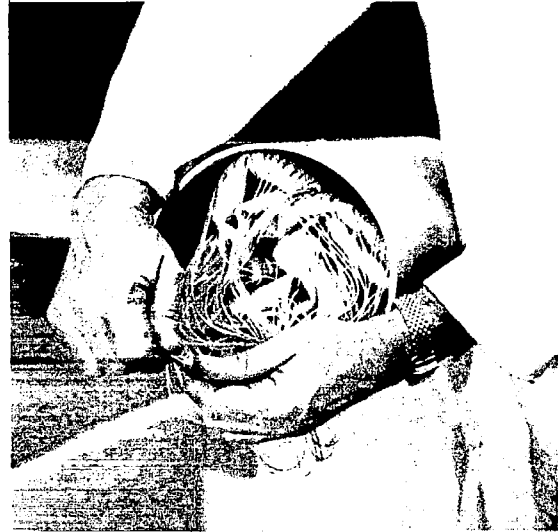
Figure 23. — Deployment Test Apparatus

Figure 24. — Results of Underwater Deployment Tests

"The aeronautical and space activities of the United States shall be conducted so as to contribute . . . to the expansion of human knowledge of phenomena in the atmosphere and space. The Administration shall provide for the widest practicable and appropriate dissemination of information concerning its activities and the results thereof."

—NATIONAL AERONAUTICS AND SPACE ACT OF 1958

NASA SCIENTIFIC AND TECHNICAL PUBLICATIONS

TECHNICAL REPORTS: Scientific and technical information considered important, complete, and a lasting contribution to existing knowledge.

TECHNICAL NOTES: Information less broad in scope but nevertheless of importance as a contribution to existing knowledge.

TECHNICAL MEMORANDUMS: Information receiving limited distribution because of preliminary data, security classification, or other reasons.

CONTRACTOR REPORTS: Scientific and technical information generated under a NASA contract or grant and considered an important contribution to existing knowledge.

TECHNICAL TRANSLATIONS: Information published in a foreign language considered to merit NASA distribution in English.

SPECIAL PUBLICATIONS: Information derived from or of value to NASA activities. Publications include conference proceedings, monographs, data compilations, handbooks, sourcebooks, and special bibliographies.

TECHNOLOGY UTILIZATION PUBLICATIONS: Information on technology used by NASA that may be of particular interest in commercial and other non-aerospace applications. Publications include Tech Briefs, Technology Utilization Reports and Notes, and Technology Surveys.

Details on the availability of these publications may be obtained from:

SCIENTIFIC AND TECHNICAL INFORMATION DIVISION

NATIONAL AERONAUTICS AND SPACE ADMINISTRATION

Washington, D.C. 20546